

A Combined FEM/MoM/GTD Technique To Analyze Elliptically Polarized Cavity-Backed Antennas With Finite Ground Plane

C. J. Reddy
Hampton University • Hampton, Virginia

M. D. Deshpande
ViGYAN, Inc. • Hampton, Virginia

D. T. Fralick
Lockheed-Martin Engineering & Sciences Company • Hampton, Virginia

C. R. Cockrell and F. B. Beck
Langley Research Center • Hampton, Virginia

Acknowledgments

The authors would like to thank Carl A. Lipp, Robert Holt, and Hunter Walden for performing the measurements on the spiral antenna.

Available electronically at the following URL address: <http://techreports.larc.nasa.gov/ltrs/ltrs.html>

Printed copies available from the following:

NASA Center for AeroSpace Information
800 Elkridge Landing Road
Linthicum Heights, MD 21090-2934
(301) 621-0390

National Technical Information Service (NTIS)
5285 Port Royal Road
Springfield, VA 22161-2171
(703) 487-4650

Abstract

Radiation pattern prediction analysis of elliptically polarized cavity-backed aperture antennas in a finite ground plane is performed using a combined finite element method/method of moments/geometrical theory of diffraction (FEM/MoM/GTD) technique. The magnetic current on the cavity-backed aperture in an infinite ground plane is calculated using the combined FEM/MoM analysis. GTD, including the slope diffraction contribution, is used to calculate the diffracted fields caused by both soft and hard polarizations at the edges of the finite ground plane. Explicit expressions for regular diffraction coefficients and slope diffraction coefficients are presented. The slope of the incident magnetic field at the diffraction points is derived and analytical expressions are presented. Numerical results for the radiation patterns of a cavity-backed circular spiral microstrip patch antenna excited by a coaxial probe in a finite rectangular ground plane are computed and compared with experimental results.

1. Introduction

Cavity-backed antennas are important to aerospace and automobile applications because of their conformal nature. A combined finite element method/method of moments/geometrical theory of diffraction (FEM/MoM/GTD) technique was applied to linearly polarized cavity-backed antennas in a finite ground plane (ref. 1). In this method, the far field caused by the magnetic current in the aperture is considered incident on the edge of the finite ground plane to produce the diffracted field. In GTD, when the electric field is normal to the edge of the ground plane it is referred to as *hard polarization* and when the electric field is tangential to the edge of the ground plane it is referred to as *soft polarization*. For soft polarization, the electric field incident at the diffraction point on the ground plane is zero, and hence the diffracted field also is zero. Physically the diffracted field does not abruptly go to zero. The higher order diffraction effect known as slope diffraction provides a nonzero diffracted field whenever the incident field is zero. In such instances, GTD may be used with slope diffraction.

This paper describes a combined FEM/MoM method used to analyze the elliptically polarized cavity-backed antennas in a finite ground plane. GTD with slope diffraction coefficients is used to augment the radiation patterns of these antennas in a finite ground plane. The slope diffraction coefficients are written explicitly assuming an aperture antenna as the source. The diffracted fields are calculated using the slope diffraction coefficient and added to the diffracted fields, which depend on the incident fields to produce the total diffracted fields (ref. 2).

A cavity-backed Archimedean spiral microstrip antenna fed by the center conductor of a coaxial line is considered in this paper. For this elliptically polarized antenna, GTD (which includes slope diffraction) is used to account for the radiation patterns of both E_θ and E_ϕ polarizations (ref. 3). The radiation patterns of the spiral antenna are calculated and compared with experimental results measured at Langley's Low Frequency Antenna Measurement Facility. Good agreement is shown between the calculated and measured data.

Section 2 of this paper describes the theory of the FEM/MoM/GTD method. Section 3 compares numerical results with experimental data to validate the FEM/MoM/GTD method, and some limitations on the numerical results and experimental data are also discussed. Section 4 presents conclusions. Expressions for regular diffraction coefficients, slope diffraction coefficients, and analytical expressions for slope of the incident field are given in the appendix.

Symbols

D_s	soft diffraction coefficient
D_h	hard diffraction coefficient
D^i	defined in equation (A16)
D^r	defined in equation (A17)
\vec{E}	electric field
E_θ	electric far field, θ component
E_ϕ	electric far field, ϕ component
E_ϕ^{sd}	ϕ -component of diffracted electric field
E_ϕ^i	ϕ -component of incident electric field
E_θ^{sd}	θ -component of diffracted electric field
E_θ^i	θ -component of incident electric field
F_s	defined in equation (A9)
g^\pm	defined in equation (A10)
\vec{H}_{ap}	magnetic field at aperture
\vec{H}_{inp}	magnetic field at input plane
H_θ^{sd}	θ -component of diffracted magnetic field
H_θ^i	θ -component of incident magnetic field
H_ϕ^{sd}	ϕ -component of diffracted magnetic field
H_ϕ^i	ϕ -component of incident magnetic field
$H_{\theta ff}$	magnetic far field, θ component
$H_{\phi ff}$	magnetic far field, ϕ component
$H_{\theta A}^d$	diffracted magnetic field at point A, θ component
$H_{\phi A}^d$	diffracted magnetic field at point A, ϕ component
$H_{\theta B}^d$	diffracted magnetic field at point B, θ component
$H_{\phi B}^d$	diffracted magnetic field at point B, ϕ component
$H_{\theta C}^d$	diffracted magnetic field at point C, θ component
$H_{\phi C}^d$	diffracted magnetic field at point C, ϕ component
$H_{\theta D}^d$	diffracted magnetic field at point D, θ component
$H_{\phi D}^d$	diffracted magnetic field at point D, ϕ component
$H_{\theta ff}^t$	total magnetic far field after adding diffracted field, θ component
$H_{\phi ff}^t$	total magnetic far field after adding diffracted field, ϕ component
j	$= \sqrt{-1}$
k_o	free space wavenumber

k_x	Fourier transform variable with respect to x
k_y	Fourier transform variable with respect to y
\vec{M}	magnetic current in aperture
M_x	x -component of magnetic current
M_y	y -component of magnetic current
\tilde{M}_x	Fourier transform of M_x , equation (7)
\tilde{M}_y	Fourier transform of M_y , equation (8)
\hat{n}	unit normal
n	defined in figure A1
N^\pm	defined in equation (A11)
Q_D	diffraction point on ground plane
r, θ, ϕ	spherical coordinates
S_{11}	return loss, dB
S_{ap}	integration over aperture surface
S_{inp}	integration over input plane
S_1	defined in equation (A26)
S_2	defined in equation (A27)
s'	distance between source and diffraction point
s	distance between diffraction point and observation point
T_1	defined in equation (A24)
T_2	defined in equation (A25)
\vec{T}	testing function
\hat{u}	unit normal in ψ' direction
V	integration over volume
w_1, w_2	dimensions of finite ground plane
x, y, z	Cartesian coordinates
ϵ_r	relative permittivity
η	intrinsic impedance of free space
μ_o	permeability of free space
μ_r	relative permeability
ξ_1, ξ_2	defined in equations (16) and (17)
ρ_{cA}, ρ_{cB}	defined in equation (15)
Φ^i	electric or magnetic incident field for soft polarization
Φ^{sd}	electric or magnetic diffracted field for soft polarization
Φ^{td}	total diffracted field for soft polarization
Ψ^i	electric or magnetic incident field for hard polarization
Ψ^{sd}	electric or magnetic diffracted field for hard polarization
Ψ^{td}	total diffracted field for hard polarization

ψ'	defined in figure A1
ω	angular frequency
∇	del operator

2. Theory

Figure 1 shows the geometry of a cavity-backed aperture in a finite ground plane. For a linear, isotropic, and source-free region the electric field satisfies the vector wave equation

$$\nabla \times \left(\frac{1}{\mu_r} \nabla \times \vec{E} \right) - k_o^2 \epsilon_r \vec{E} = 0 \quad (1)$$

where μ_r and ϵ_r are the relative permeability and permittivity, respectively, of the medium in the cavity. The time variation $\exp(j\omega t)$ is assumed and suppressed throughout this paper.

To facilitate the solution of the partial differential equation in equation (1) for the cavity using the FEM method, equation (1) is multiplied by a vector testing function \vec{T} and the result is integrated over the volume of the cavity. By applying suitable vector identities, equation (1) can be written in its weak form (ref. 4) as

$$\iiint_V \frac{1}{\mu_r} (\nabla \times \vec{T}) \cdot (\nabla \times \vec{E}) dv - k_o^2 \epsilon_r \iiint_V \vec{T} \cdot \vec{E} dv = \iiint_V \nabla \cdot \left(\vec{T} \times \frac{1}{\mu_r} \nabla \times \vec{E} \right) dv \quad (2)$$

By applying the divergence theorem to the integral on the right hand side of equation (2) and using Maxwell's equation $\nabla \times \vec{E} = -j\omega\mu_o\mu_r\vec{H}$, where μ_o is the permeability of free space and ω is the angular frequency, equation (2) can be rewritten as

$$\iiint_V \frac{1}{\mu_r} (\nabla \times \vec{T}) \cdot (\nabla \times \vec{E}) dv - k_o^2 \epsilon_r \iiint_V \vec{T} \cdot \vec{E} dv = j\omega\mu_o \iint_S (\vec{T} \times \hat{n}) \cdot \vec{H} ds \quad (3)$$

where \hat{n} is the unit outward normal to the surface and \vec{H} is the magnetic field on the surface of the cavity. Since the tangential electric field is zero on the perfect electric conducting (PEC) walls of the cavity, the surface integral in equation (3) is nonzero only over the aperture opening in the infinite ground plane and the input aperture.

$$\iiint_V \frac{1}{\mu_r} (\nabla \times \vec{T}) \cdot (\nabla \times \vec{E}) dv - k_o^2 \epsilon_r \iiint_V \vec{T} \cdot \vec{E} dv - j\omega\mu_o \iint_{S_{ap}} (\vec{T} \times \hat{n}) \cdot \vec{H}_{ap} ds = j\omega\mu_o \iint_{S_{inp}} (\vec{T} \times \hat{n}) \cdot \vec{H}_{inp} ds \quad (4)$$

where S_{ap} is the aperture surface, S_{inp} is the input surface (see fig. 1), \vec{H}_{ap} is the magnetic field at the aperture, and \vec{H}_{inp} is the magnetic field at the input surface.

At this point, equation (4) can be divided into three parts. The first part discretizes and evaluates volume integrals on the left hand side of equation (4) and the second part discretizes and evaluates the surface integral over S_{ap} . The third part involves the surface integral over the input aperture. The volume integral is evaluated by discretizing the volume of the cavity with tetrahedral elements and evaluating the integral over the volume of each tetrahedral element (ref. 5). These element volume integral contributions are added over all tetrahedral elements to form a sparse matrix. The second integral is evaluated over the surface of the aperture. The discretization of the volume of the cavity into tetrahedral elements automatically discretizes the aperture surface into triangular elements. Assuming current basis functions similar to those described in reference 6, an integral equation is formed, which contributes to the dense part of the system matrix. Image theory is used to account for the presence of the infinite ground plane. The third integral is evaluated over the input coaxial aperture surface and forms the exci-

tation column matrix. Solving for the system matrix formed by these three integrals obtains the electric fields in the cavity and hence the magnetic current \vec{M} in the aperture S_{ap} .

Using the magnetic current $\vec{M}(x, y)$ over the aperture, the magnetic far field is given by the following equations:

$$H_{\theta ff}(r, \theta, \phi) = -\frac{jk_o \exp(-jk_o r)}{\eta} \frac{1}{2\pi r} \cos \theta \left[\tilde{M}_x(k_x, k_y) \cos \phi + \tilde{M}_y(k_x, k_y) \sin \phi \right] \quad (5)$$

$$H_{\phi ff}(r, \theta, \phi) = -\frac{jk_o \exp(-jk_o r)}{\eta} \frac{1}{2\pi r} \left[\tilde{M}_y(k_x, k_y) \cos \phi - \tilde{M}_x(k_x, k_y) \sin \phi \right] \quad (6)$$

where

$$\tilde{M}_x(k_x, k_y) = \iint_{S_a} M_x(x, y) \exp[j(k_x x + k_y y)] dx dy \quad (7)$$

and

$$\tilde{M}_y(k_x, k_y) = \iint_{S_a} M_y(x, y) \exp[j(k_x x + k_y y)] dx dy \quad (8)$$

$$k_x = k_o \cos \phi \sin \theta \quad (9)$$

$$k_y = k_o \sin \phi \sin \theta \quad (10)$$

Radiation patterns in the forward direction of a cavity-backed antenna in an infinite ground plane are computed using equations (5) and (6). The effect of the finite ground plane is incorporated by employing the edge diffraction coefficients with the slope diffraction coefficients. The radiation fields are supplemented by the additional field contributions occurring from the diffraction by the edges of the finite ground plane. The diffracted field supplements the field in the forward direction, whereas it accounts totally for the field in the shadow region (behind the finite ground plane) where the infinite ground plane solution gives a zero field.

Figure 1 illustrates the geometry of the finite ground plane. The midpoints on the two edges of length W_2 are given by A and B and the midpoints on the two edges of length W_1 are given by C and D. The total diffracted fields at A and B are given by (refs. 2, 7, and 8)

$$H_{\theta A}^d \approx \frac{1}{2} \left[H_{\theta ff} \left(d_r, \frac{\pi}{2}, 0 \right) D_s(\rho_{cA}, \xi_1, \psi', \beta'_o, n) + \frac{1}{jk_o} \left(\frac{\partial H_{\theta ff}}{\partial \theta} \right) \bigg|_{d_r, \frac{\pi}{2}, 0} \left(\frac{\partial D_s}{\partial \psi'} \right) \bigg|_{\rho_{cA}, \xi_1, \psi', \beta'_o, n} \right] \\ \times \left(\frac{\rho_{cA}}{r} \right)^{1/2} \exp(-jk_o r) \exp(jk_o d_r \sin \theta) \quad (11)$$

$$H_{\theta B}^d \approx \frac{1}{2} \left[H_{\theta ff} \left(d_r, \frac{\pi}{2}, \pi \right) D_s(\rho_{cB}, \xi_2, \psi', \beta'_o, n) + \frac{1}{jk_o} \left(\frac{\partial H_{\theta ff}}{\partial \theta} \right) \bigg|_{d_r, \frac{\pi}{2}, \pi} \left(\frac{\partial D_s}{\partial \psi'} \right) \bigg|_{\rho_{cB}, \xi_2, \psi', \beta'_o, n} \right] \\ \times \left(\frac{\rho_{cA}}{r} \right)^{1/2} \exp(-jk_o r) \exp(-jk_o d_r \sin \theta) \quad (12)$$

for ϕ polarization, and

$$H_{\phi A}^d \approx \frac{1}{2} \left[H_{\phi ff} \left(d_r, \frac{\pi}{2}, 0 \right) D_h(\rho_{cA}, \xi_1, \psi', \beta'_o, n) + \frac{1}{jk_o} \left(\frac{\partial H_{\phi ff}}{\partial \theta} \right) \bigg|_{d_r, \frac{\pi}{2}, 0} \left(\frac{\partial D_h}{\partial \psi'} \right) \bigg|_{\rho_{cA}, \xi_1, \psi', \beta'_o, n} \right] \\ \times \left(\frac{\rho_{cA}}{r} \right)^{1/2} \exp(-jk_o r) \exp(jk_o d_r \sin \theta) \quad (13)$$

$$H_{\phi B}^d \approx \frac{1}{2} \left[H_{\phi ff} \left(d_r, \frac{\pi}{2}, \pi \right) D_h(\rho_{cB}, \xi_2, \psi', \beta'_o, n) + \frac{1}{jk_o} \left(\frac{\partial H_{\phi ff}}{\partial \theta} \right) \bigg|_{d_r, \frac{\pi}{2}, \pi} \left(\frac{\partial D_h}{\partial \psi'} \right) \bigg|_{\rho_{cB}, \xi_2, \psi', \beta'_o, n} \right] \\ \times \left(\frac{\rho_{cA}}{r} \right)^{1/2} \exp(-jk_o r) \exp(-jk_o d_r \sin \theta) \quad (14)$$

for θ polarization. In equations (11)–(14),

$$\rho_{cA} = \rho_{cB} = d_r = r = \frac{W_1}{2} \quad (15)$$

and

$$\xi_1 = \frac{\pi}{2} + \theta \quad (0 \leq \theta \leq \pi) \quad (16)$$

$$\xi_2 = \begin{cases} \frac{\pi}{2} - \theta & (0 \leq \theta < \frac{\pi}{2}) \\ \frac{5\pi}{2} - \theta & (\frac{\pi}{2} < \theta \leq \pi) \end{cases} \quad (17)$$

Here, ψ' = Angle of incidence from the aperture (source) toward the point of diffraction (A or B) = 0° , $\beta'_o = \pi/2$ for normal incidence (ref. 7, p. 811), and n = Wedge factor (ref. 7, figs. 13–30).

Similarly, the diffracted fields at C and D are also calculated by replacing $\rho_{cC} = \rho_{cD} = d_r = r = W_2/2$. The detailed expressions for diffraction coefficients $D_{s/h}$ are given in reference 7 (eqs. (13)–(89)). The expressions for the slope diffraction coefficients and the slope of the incident magnetic field at the diffraction points are given in the appendix. The total diffracted field is given by

$$H_\theta^d = \begin{cases} H_{\theta A}^d + H_{\theta B}^d & (\phi = 0^\circ \text{ plane}) \\ H_{\theta C}^d + H_{\theta D}^d & (\phi = 90^\circ \text{ plane}) \end{cases} \quad (18)$$

and

$$H_\phi^d = \begin{cases} H_{\phi A}^d + H_{\phi B}^d & (\phi = 0^\circ \text{ plane}) \\ H_{\phi C}^d + H_{\phi D}^d & (\phi = 90^\circ \text{ plane}) \end{cases} \quad (19)$$

The diffracted fields for $\phi = 180^\circ$ and $\phi = 270^\circ$ planes can also be calculated in a similar manner as described for the $\phi = 0^\circ$ and $\phi = 90^\circ$ planes. The total radiated far field is given by adding the diffracted magnetic field and magnetic far field given in equations (5) and (6):

$$H'_{\theta ff} = H_{\theta ff} + H_{\theta}^d \quad (20)$$

$$H'_{\phi ff} = H_{\phi ff} + H_{\phi}^d \quad (21)$$

The radiated electric far field is given by

$$E_{\theta} = \eta H'_{\phi ff} \quad (22)$$

$$E_{\phi} = \eta H'_{\theta ff} \quad (23)$$

Using the magnetic current in the aperture in equations (5) and (6) and evaluating equations (20)–(23), the radiation patterns of the cavity-backed aperture antennas with a finite rectangular ground plane are computed.

3. Numerical and Experimental Results

To verify the validity of the analysis presented, a cavity-backed spiral microstrip antenna in a finite rectangular ground plane is considered. Figure 2 shows the geometry of the spiral antenna. A 2 1/2 turn, 2-arm circular Archimedean spiral is fed at the center by the center conductor of the coaxial probe. The substrate is 1/16 in. thick with a relative dielectric constant of 2.33. The width of the spiral is 2/23 in. The microstrip spiral antenna is placed in a 2-in.-diameter cavity of 1/16 in. depth with a rectangular ground plane with a 24-in. length and 12-in. width.

3.1. Experimental Procedure

The spiral antenna was fed at its center with the center conductor made of RG-141 coaxial semi-rigid cable. The copper shield was conductively bonded to the copper clad backside of the antenna. This backside provided a conductive path to the ground plane when placed in the machined cavity in the ground plane. The antenna/ground plane assembly was then placed on the rollover azimuth over-elevation positioning system in the Langley Low Frequency Antenna Measurement Facility.

Electrical boresight was accomplished by sighting the characteristic null, normal to the plane of the antenna, of a spiral fed in the manner described in the previous paragraph. Calibration of the system was not performed. All radiation pattern plots were normalized to the respective peak values.

Principal plane measurements were accomplished for both horizontal (E_{θ}) and vertical (E_{ϕ}) polarizations and for two orthogonal positions of the antenna, $\phi = 0^\circ, 180^\circ$ and $\phi = 90^\circ, 270^\circ$, for the $\phi = 0^\circ, 180^\circ$ plane (fig. 2).

3.2. Numerical Modelling

The cavity volume with the spiral antenna is modelled using a commercial package COSMOS/M (ref. 9) and meshed with 8740 tetrahedral elements, resulting in 1820 triangular elements in the aperture surface. For proper representation of the electric field, the number of tetrahedrals required depends on the intended sampling rate of the electric field at a particular frequency. The radiation patterns for both horizontal (E_{θ}) polarization and vertical (E_{ϕ}) polarization are computed using equations (20) and (21), respectively. Figures 3(a) and (b) are plots of normalized radiation patterns for horizontal polarization at $\phi = 0^\circ, 180^\circ$ and $\phi = 90^\circ, 270^\circ$, respectively, at 4 GHz. Figures 3(a) and (b) show very good agreement between the measured data and the computed results.

Figures 4(a) and (b) are plots of normalized radiation patterns for vertical polarization at $\phi = 0^\circ, 180^\circ$ and $\phi = 90^\circ, 270^\circ$, respectively, at 4 GHz. Good agreement between the computed and

experimental results is found in the forward direction of the antenna. There is poor agreement of the results in the backward direction. Possible causes for this poor agreement are discussed in section 3.3. Similarly, computed results are plotted with the experimental data for normalized radiation patterns for both horizontal and vertical polarizations in figures 5 and 6, respectively, at 5 GHz.

3.3. Experimental Limitations

Two primary contributions should be mentioned as possible sources of measurement error. The first is the poor return loss, S_{11} , of the spiral antenna used in the measurement. The antenna, fed as previously described with no balun or matching network, was matched poorly to the 50Ω measurement system. A Wheeler can test (ref. 10) indicated that most of the measurable return loss could be attributed to factors other than radiation resistance. Therefore, only small signal levels were coupled to the coaxial line feeding the antenna, and this lack of adequate signal levels caused a degradation of overall system dynamic range of the measurement setup.

The second contributor to the inaccuracy was caused by the placement of the remote mixer and relatively low signal levels mentioned in the previous paragraph. Standard practice is to place the mixer as close as possible to the antenna being tested. The mixer for these measurements was placed behind the ground plane, so that losses at the desired test frequency could be minimized. As a consequence, the mixer and the cable were directly illuminated for angles of $\theta \geq 90^\circ$. Although the cable and mixer were both shielded, neither the shielding to the cable nor the shielding to the mixer were perfect. This factor, along with an already small desired signal level on the cable due to mismatch and position relative to the main lobe of the antenna, helps explain some of the differences between the measured and computed results for angles of $\theta \geq 90^\circ$. Further experimentation possibilities include designing a feed network to properly match the antenna and using absorber around the remote mixer if necessary.

3.4. Computational Limitations

Because of the relatively small thickness of the substrate of the spiral antenna, the volume of the cavity must be meshed with a good quality tetrahedral mesh. To account for the rapid variation of the field in the cavity, it is essential that several layers of elements be present to accurately account for the field variation. This requires a large number of tetrahedral elements and a proportionately large number of triangular elements in the aperture surface, which results in a large number of nonzero elements in the system matrix. As the frequency increases, the electrical depth of the cavity increases as the wavelength decreases, which in turn requires smaller tetrahedral elements to meet the field sampling requirement. Hence, the computations are limited to 4 and 5 GHz for the cases investigated here. With proper meshing and availability of computational facilities such as parallel computing, this antenna configuration can be accurately analyzed at higher frequencies using FEM/MoM analysis.

4. Conclusions

An analysis of cavity-backed elliptically polarized aperture antennas in a finite rectangular ground plane is carried out using a combined finite element method/method of moments/geometrical theory of diffraction (FEM/MoM/GTD) technique. Slope diffraction coefficients are successfully used to account for the diffracted field of soft polarization, whose incident field at the diffraction point is zero. Analytical expressions for slope of the incident field are derived, avoiding the numerical differentiation of the incident field at the diffraction points. The radiation patterns for a circular Archimedean spiral microstrip antenna are computed with a finite rectangular ground plane and compared with the experimental data. Both the computed and measured radiation patterns show very good agreement within the computational and experimental limitations, validating the analysis presented in this paper.

Appendix

Use of Slope Diffraction Coefficients for Aperture Antennas on Finite Ground Planes

For clarity in explaining slope diffraction, the cavity-backed aperture is raised above the conducting surface (fig. A1). From Balanis (ref. 7) with appropriate notation change, the slope diffracted fields from point Q_D are written as

$$\Phi^{sd} = \frac{1}{jk_o} \left(\frac{\partial \Phi^i}{\partial u} \right)_{Q_D} \left(\frac{\partial D_s}{\partial \Psi'} \right) \frac{\sqrt{s'}}{s} \exp(-jk_o s) \quad (\text{A1})$$

for soft polarization where

$$\left. \frac{\partial \Phi^i}{\partial u} \right|_{Q_D} = \hat{u} \cdot \nabla \Phi^i = \text{Slope of incident field} \quad (\text{A2})$$

$$\frac{\partial D_s}{\partial \Psi'} = \text{Slope diffraction coefficient} \quad (\text{A3})$$

and $\Phi^{sd}(\Phi^i)$ represent either $E_\phi^{sd}(E_\phi^i)$ or $H_\theta^{sd}(H_\theta^i)$, respectively. Similarly for hard polarization

$$\Psi^{sd} = \frac{1}{jk_o} \left(\frac{\partial \Psi^i}{\partial u} \right)_{Q_D} \left(\frac{\partial D_h}{\partial \Psi'} \right) \frac{\sqrt{s'}}{s} \exp(-jk_o s) \quad (\text{A4})$$

where

$$\left. \frac{\partial \Psi^i}{\partial u} \right|_{Q_D} = \hat{u} \cdot \nabla \Psi^i = \text{Slope of incident field} \quad (\text{A5})$$

$$\frac{\partial D_h}{\partial \Psi'} = \text{Slope diffraction coefficient} \quad (\text{A6})$$

and $\Psi^{sd}(\Psi^i)$ represent either $E_\theta^{sd}(E_\theta^i)$ or $H_\phi^{sd}(H_\phi^i)$, respectively.

The general diffraction coefficients for the soft and hard polarizations are given by Balanis (ref. 7). These coefficients are written in the notation of the present paper as

$$\begin{aligned} \frac{\partial D_s}{\partial \Psi'} = & -\frac{\exp\left(-j\frac{\pi}{4}\right)}{4n^2 \sqrt{2\pi k_o}} \left(\left\{ \csc^2 \left[\frac{\pi + (\Psi - \Psi')}{2n} \right] F_s \left[k_o s' g^+(\Psi - \Psi') \right] - \csc^2 \left[\frac{\pi - (\Psi - \Psi')}{2n} \right] F_s \left[k_o s' g^-(\Psi - \Psi') \right] \right\} \right. \\ & \left. + \left\{ \csc^2 \left[\frac{\pi + (\Psi + \Psi')}{2n} \right] F_s \left[k_o s' g^+(\Psi + \Psi') \right] - \csc^2 \left[\frac{\pi - (\Psi + \Psi')}{2n} \right] F_s \left[k_o s' g^-(\Psi + \Psi') \right] \right\} \right) \end{aligned} \quad (\text{A7})$$

$$\begin{aligned} \frac{\partial D_h}{\partial \Psi'} = & -\frac{\exp\left(-j\frac{\pi}{4}\right)}{4n^2 \sqrt{2\pi k_o}} \left(\left\{ \csc^2 \left[\frac{\pi + (\Psi - \Psi')}{2n} \right] F_s \left[k_o s' g^+(\Psi - \Psi') \right] - \csc^2 \left[\frac{\pi - (\Psi - \Psi')}{2n} \right] F_s \left[k_o s' g^-(\Psi - \Psi') \right] \right\} \right. \\ & \left. - \left\{ \csc^2 \left[\frac{\pi + (\Psi + \Psi')}{2n} \right] F_s \left[k_o s' g^+(\Psi + \Psi') \right] - \csc^2 \left[\frac{\pi - (\Psi + \Psi')}{2n} \right] F_s \left[k_o s' g^-(\Psi + \Psi') \right] \right\} \right) \end{aligned} \quad (\text{A8})$$

where

$$F_s[k_o s' g^\pm(\psi \pm \psi')] = 2j \sqrt{k_o s' g^\pm(\psi \pm \psi')} \int_{\sqrt{k_o s' g^\pm(\psi \pm \psi')}}^{\infty} \frac{\exp(-j\tau)}{\sqrt{k_o s' g^\pm(\psi \pm \psi')}} d\tau \quad (\text{A9})$$

$$g^\pm(\psi \pm \psi') = 1 + \cos[(\psi \pm \psi') - 2\pi n N^\pm] \quad (\text{A10})$$

$$2\pi n N^\pm - (\psi \pm \psi') = \pm\pi \quad (\text{A11})$$

and N^\pm are the integer values which most closely satisfy the equalities.

The total diffracted field from point Q_D is given by

$$\Phi^{td} = \left[\Phi^i D_s + \frac{1}{jk_o} \left(\frac{\partial \Phi^i}{\partial u} \right)_{Q_D} \right] \left(\frac{\partial D_s}{\partial \psi'} \right) \frac{\sqrt{s'}}{s} \exp(-jk_o s) \quad (\text{A12})$$

for soft polarization and

$$\Psi^{td} = \left[\Psi^i D_h + \frac{1}{jk_o} \left(\frac{\partial \Psi^i}{\partial u} \right)_{Q_D} \right] \left(\frac{\partial D_h}{\partial \psi'} \right) \frac{\sqrt{s'}}{s} \exp(-jk_o s) \quad (\text{A13})$$

for hard polarization. For completeness, the diffraction coefficients D_s and D_h are also given below:

$$D_s = D^i - D^r \quad (\text{A14})$$

$$D_h = D^i + D^r \quad (\text{A15})$$

where

$$D^i = -\frac{\exp\left(-j\frac{\pi}{4}\right)}{2n\sqrt{2\pi k_o}} \left\{ \cot\left[\frac{\pi + (\psi - \psi')}{2n}\right] F_s[k_o s' g^+(\psi - \psi')] + \cot\left[\frac{\pi - (\psi - \psi')}{2n}\right] F_s[k_o s' g^-(\psi - \psi')] \right\} \quad (\text{A16})$$

$$D^r = -\frac{\exp\left(-j\frac{\pi}{4}\right)}{2n\sqrt{2\pi k_o}} \left\{ \cot\left[\frac{\pi + (\psi + \psi')}{2n}\right] F_s[k_o s' g^+(\psi + \psi')] + \cot\left[\frac{\pi - (\psi + \psi')}{2n}\right] F_s[k_o s' g^-(\psi + \psi')] \right\} \quad (\text{A17})$$

The remaining task is to find the incident field either as the magnetic field or the electric field. The magnetic incident field is assumed to be the far field at the diffraction point Q_D due to the magnetic current $\vec{M}(x, y)$ at the aperture and is given in equations (5) and (6) and reproduced here for the sake of continuity.

$$H_\theta^i(r, \theta, \phi) = -\frac{jk_o \exp(-jk_o r)}{\eta} \cos \theta \left[\tilde{M}_x(k_x, k_y) \cos \phi + \tilde{M}_y(k_x, k_y) \sin \phi \right] \Big|_{Q_D} \quad (\text{A18})$$

$$H_\phi^i(r, \theta, \phi) = -\frac{jk_o \exp(-jk_o r)}{\eta} \left[\tilde{M}_y(k_x, k_y) \cos \phi - \tilde{M}_x(k_x, k_y) \sin \phi \right] \Big|_{Q_D} \quad (\text{A19})$$

From figure A1, it may be noted that at the diffraction point Q_D ,

$$r = s' = \sqrt{d^2 + D^2}$$

$$\theta = \psi' + 90^\circ$$

$$\phi = 90^\circ$$

In equations (A18) and (A19), image theory is used to account for the aperture in an infinite ground plane.

In terms of the field variable θ , the slope of the incident magnetic field is written for soft polarization as

$$\frac{\partial H_\theta^i}{\partial u} = -\frac{1}{s'} \frac{\partial H_\theta^i}{\partial \theta} \quad (\text{A20})$$

and for hard polarization as

$$\frac{\partial H_\phi^i}{\partial u} = -\frac{1}{s'} \frac{\partial H_\phi^i}{\partial \theta} \quad (\text{A21})$$

Using the expressions in equations (A18) and (A19), the partial derivative with respect to θ can be written explicitly as

$$\frac{\partial H_\theta^i}{\partial \theta} = \frac{jk_o}{\eta} \frac{\exp(-jk_o r)}{2\pi r} \left[(T_1 \cos \phi + T_2 \sin \phi) \sin \theta - (S_1 \cos \phi + S_2 \sin \phi) \cos \theta \right] \quad (\text{A22})$$

$$\frac{\partial H_\phi^i}{\partial \theta} = -\frac{jk_o}{\eta} \frac{\exp(-jk_o r)}{2\pi r} \left[S_2 \cos \phi - S_1 \sin \phi \right] \quad (\text{A23})$$

where

$$T_1 = \tilde{M}_x(k_x, k_y) \quad (\text{A24})$$

$$T_2 = \tilde{M}_y(k_x, k_y) \quad (\text{A25})$$

$$S_1 = \iint_{S_a} M_x(x, y) \left[jk_o (x \cos \phi + y \sin \phi) \cos \theta \right] \exp \left[j(k_x x + k_y y) \right] dx dy \quad (\text{A26})$$

$$S_2 = \iint_{S_a} M_y(x, y) \left[jk_o (x \cos \phi + y \sin \phi) \cos \theta \right] \exp \left[j(k_x x + k_y y) \right] dx dy \quad (\text{A27})$$

In writing equations (A26) and (A27), Leibnitz's rule of differentiating under the integral sign is utilized (ref. 11).

Allowing the aperture to be lowered to the conducting plane, the slope incident magnetic fields can be computed from equations (A22) and (A23) with equations (A24), (A25), (A26), and (A27) for $d = 0$ and $\psi' = 0^\circ$. The total diffracted magnetic fields can then be computed using either equation (A12) or (A13), depending on the polarization.

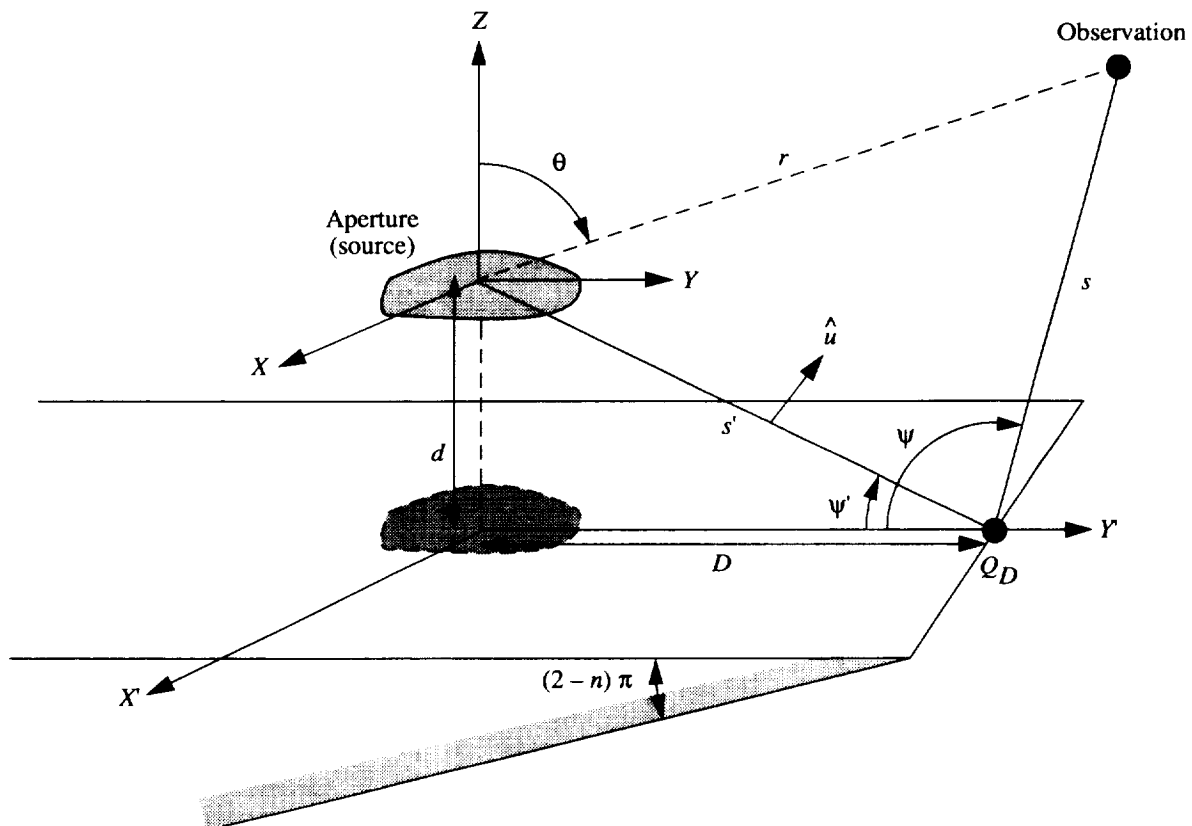


Figure A1. Geometry of aperture in finite ground plane.

References

1. Reddy, C. J.; Deshpande, M. D.; Cockrell, C. R.; and Beck, F. B.: *Analysis of Three-Dimensional-Cavity-Backed Aperture Antennas Using a Combined Finite Element Method/Method of Moments/Geometrical Theory of Diffraction Technique*. NASA TP-3548, 1995.
2. Cockrell, C. R.; and Beck F. B.: *Note on Use of Slope Diffraction Coefficients for Aperture Antennas on Finite Ground Plane*. NASA TM-110192, 1995.
3. Reddy, C. J.; Deshpande, M. D.; and Fralick, D. T.: *Analysis of Elliptically Polarized Cavity-Backed Antennas Using a Combined FEM/MoM/GTD Technique*. NASA CR-198197, 1995.
4. Jin, Jianming: *The Finite Element Method in Electromagnetics*. John Wiley & Sons, Inc., 1993.
5. Reddy, C. J.; Deshpande, Manohar D.; Cockrell, C. R.; and Beck, F. B.: *Finite Element Method for Eigenvalue Problems in Electromagnetics*. NASA TP-3485, 1994.
6. Rao, Sadasiva M.; Wilton, Donald R.; and Glisson, Allen W.: Electromagnetic Scattering by Surfaces of Arbitrary Shape. *IEEE Trans. Antennas Propagat.*, vol. AP-30, no. 3, May 1982, pp. 409–418.
7. Balanis, Constantine A.: *Advanced Engineering Electromagnetics*. John Wiley & Sons, Inc., 1989.
8. Cockrell, C. R.; and Pathak, Prabhakar: Diffraction Theory Techniques Applied to Aperture Antennas on Finite Circular and Square Ground Planes. *IEEE Trans. Antennas Propagat.*, vol. AP-22, no. 3, May 1974, pp. 443–448.
9. *COSMOS/M User Guide*. Structural Research and Analysis Corp., 1993.
10. Wheeler, Harold A.: The Radiansphere Around a Small Antenna. *Proc. IRE*, 1959, pp. 1325–1331.
11. Arfken, George: *Mathematical Methods for Physicists*. Academic Press, Inc., 1985.

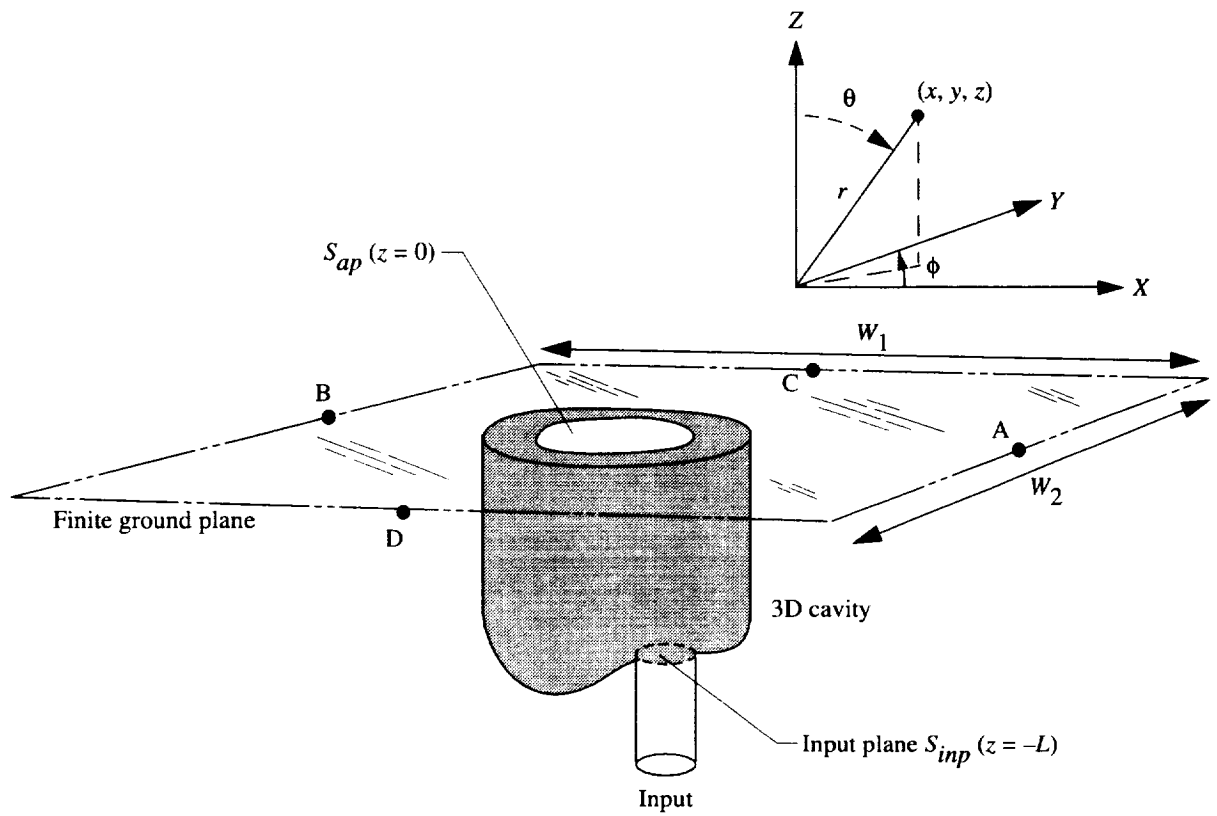


Figure 1. Geometry of cavity-backed aperture in finite ground plane.

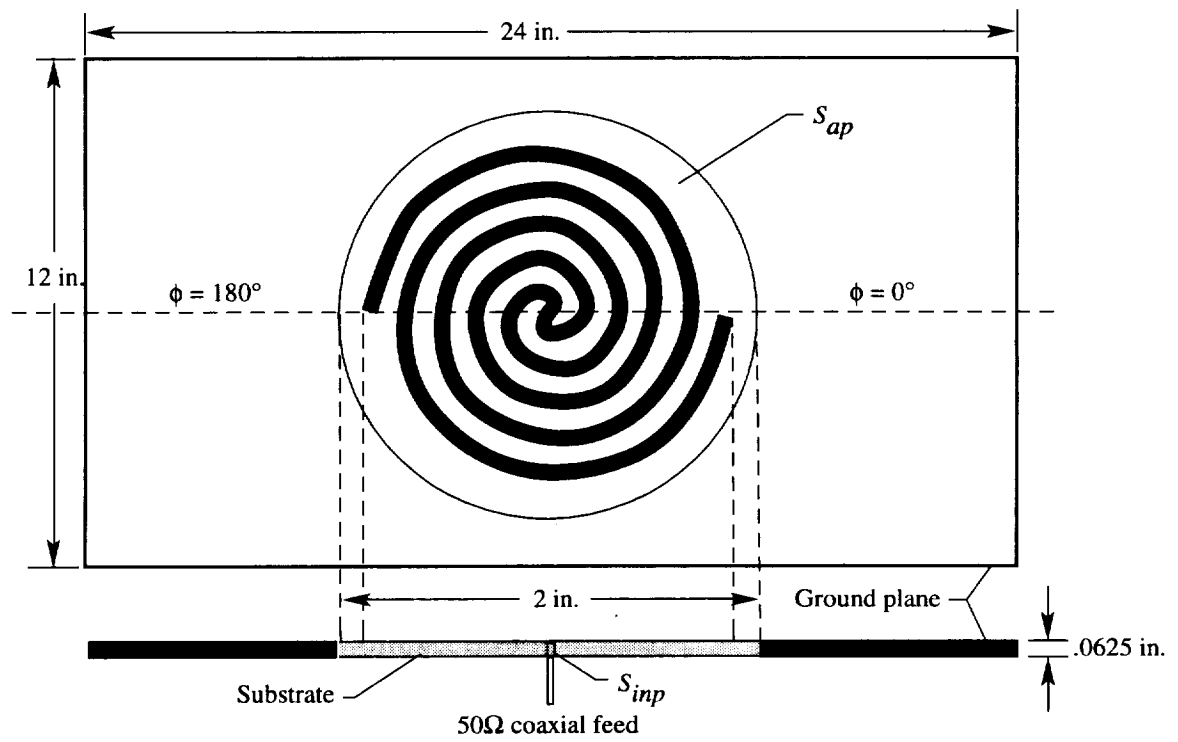
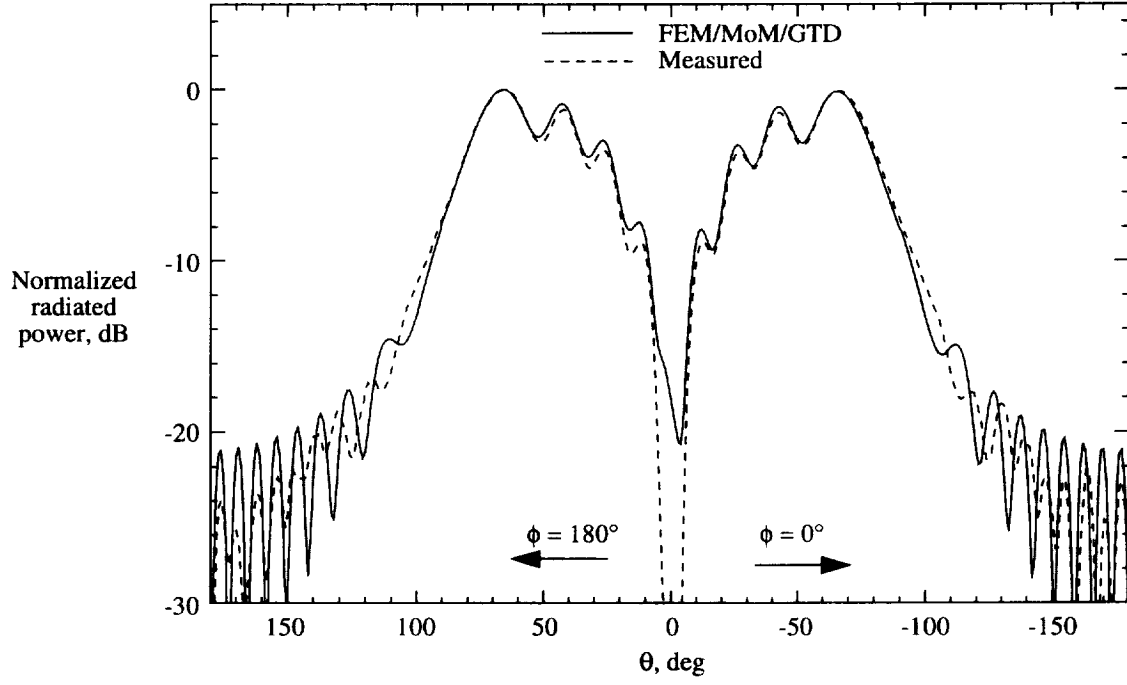
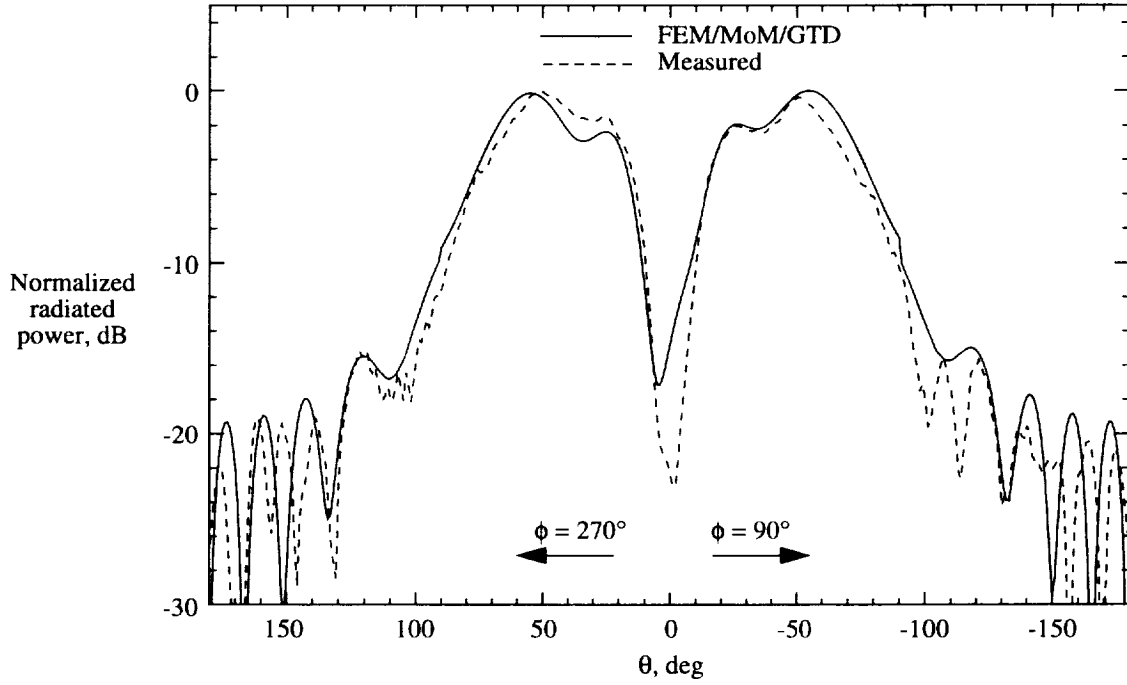


Figure 2. Cavity-backed spiral microstrip antenna in finite ground plane.

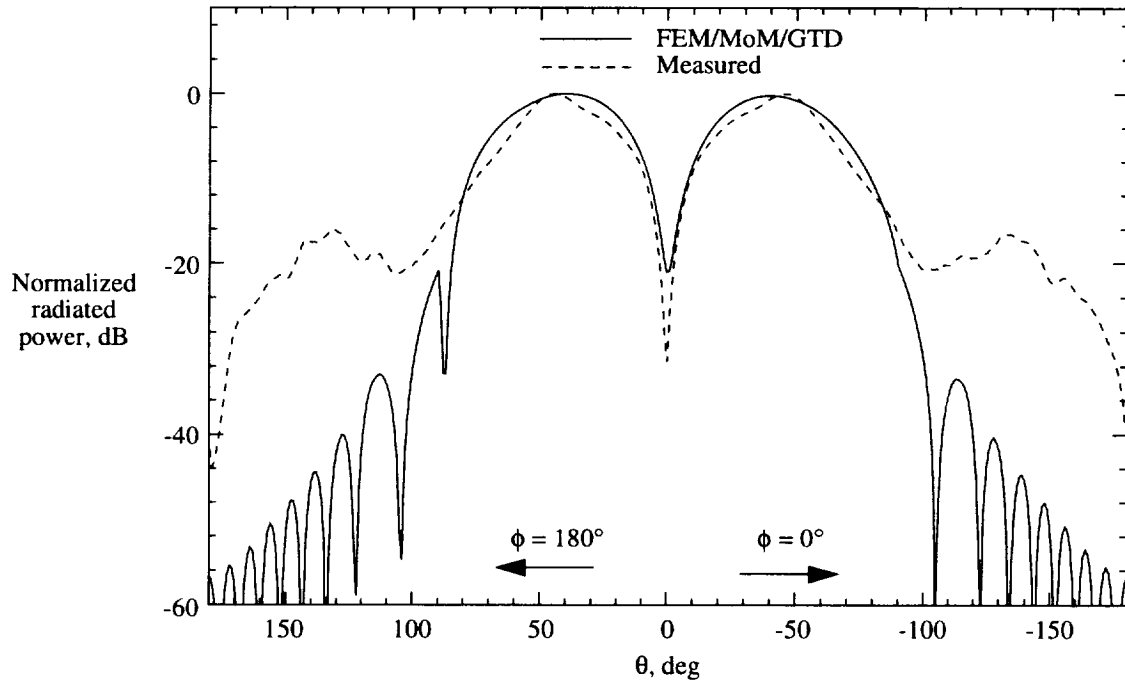


(a) Horizontal (E_θ) polarization at $\phi = 0^\circ$ and $\phi = 180^\circ$.

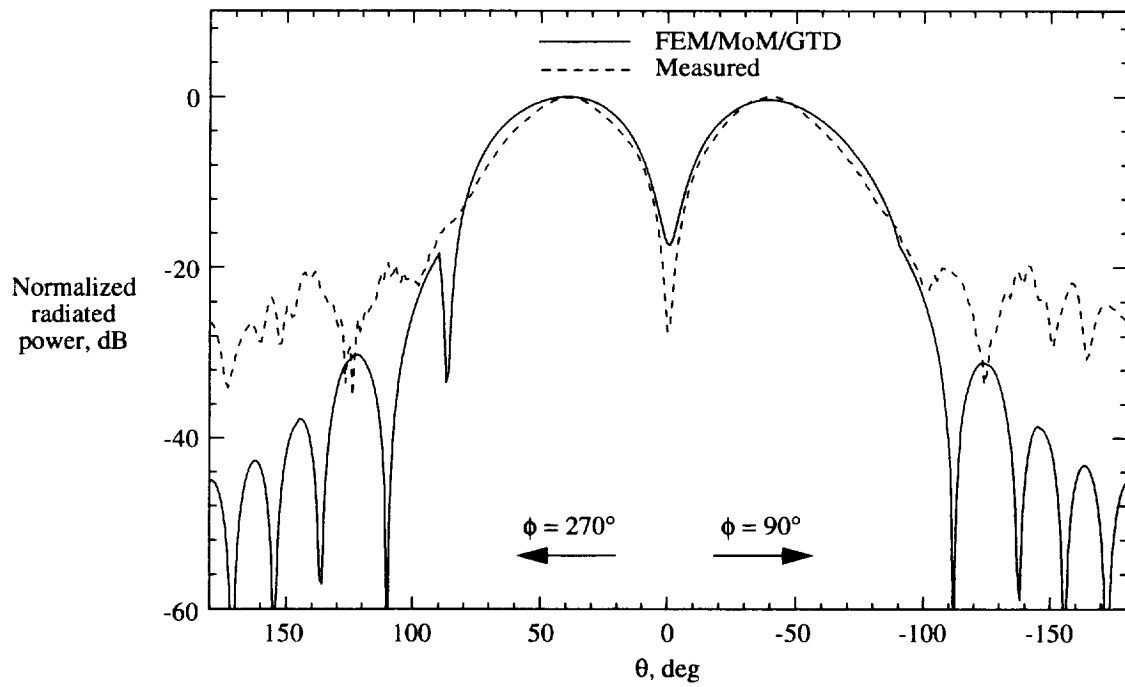


(b) Horizontal (E_θ) polarization at $\phi = 90^\circ$ and $\phi = 270^\circ$.

Figure 3. Radiation patterns of spiral antenna at 4 GHz.

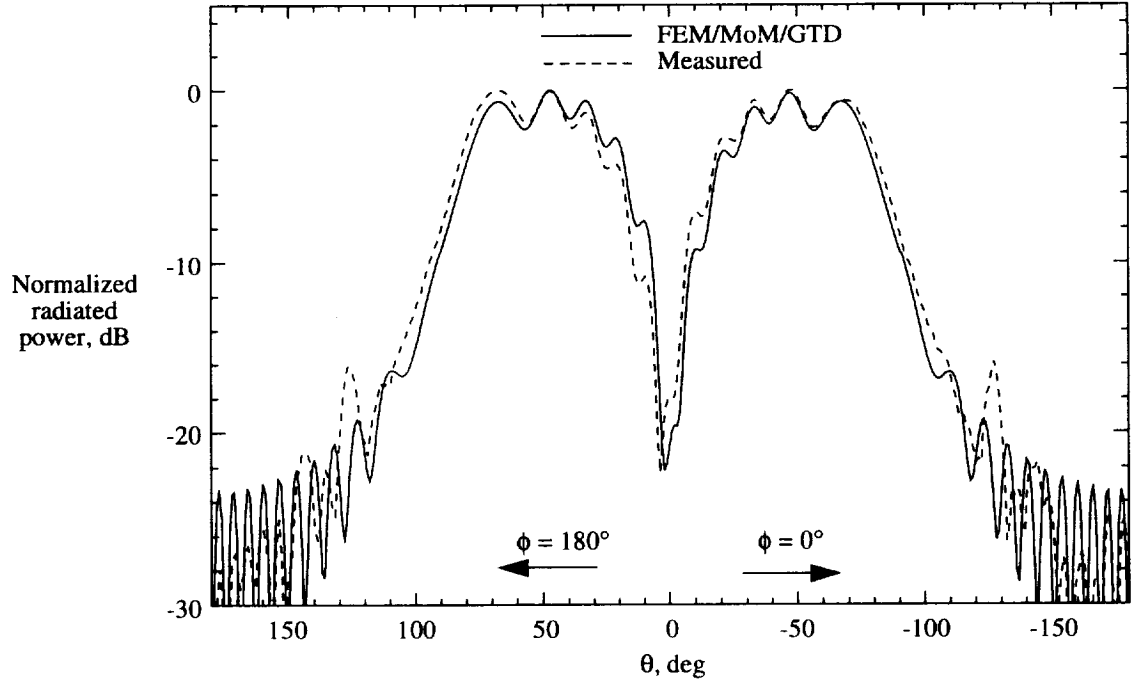


(a) Vertical (E_ϕ) polarization at $\phi = 0^\circ$ and $\phi = 180^\circ$.

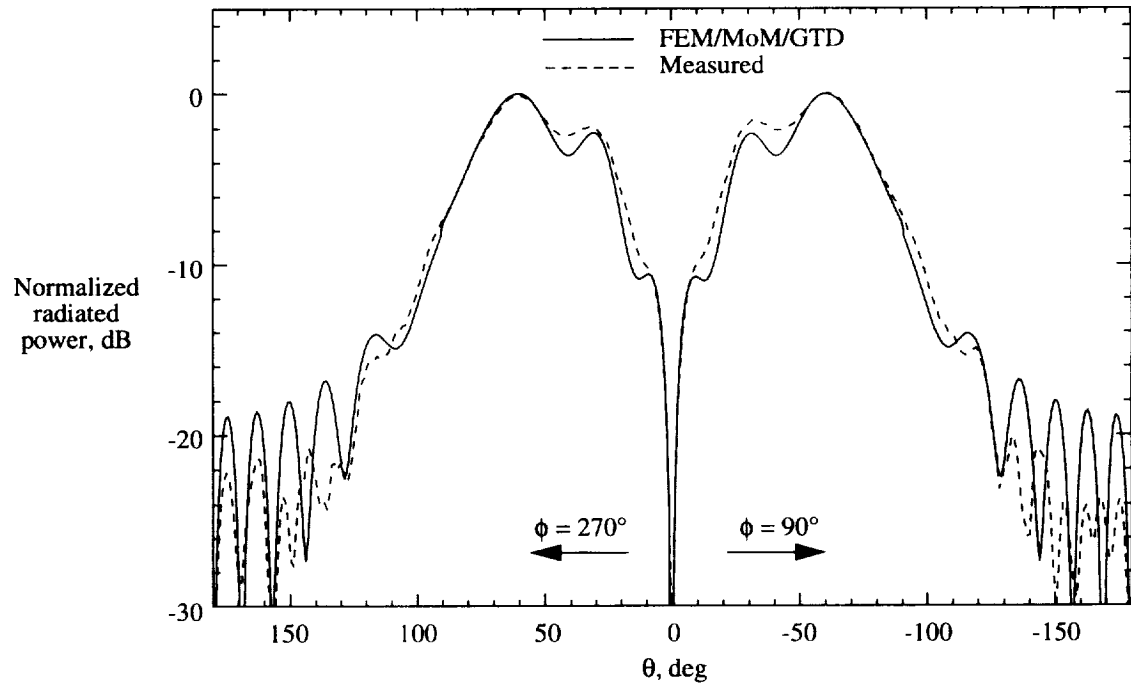


(b) Vertical (E_ϕ) polarization at $\phi = 90^\circ$ and $\phi = 270^\circ$.

Figure 4. Radiation patterns of spiral antenna at 4 GHz.

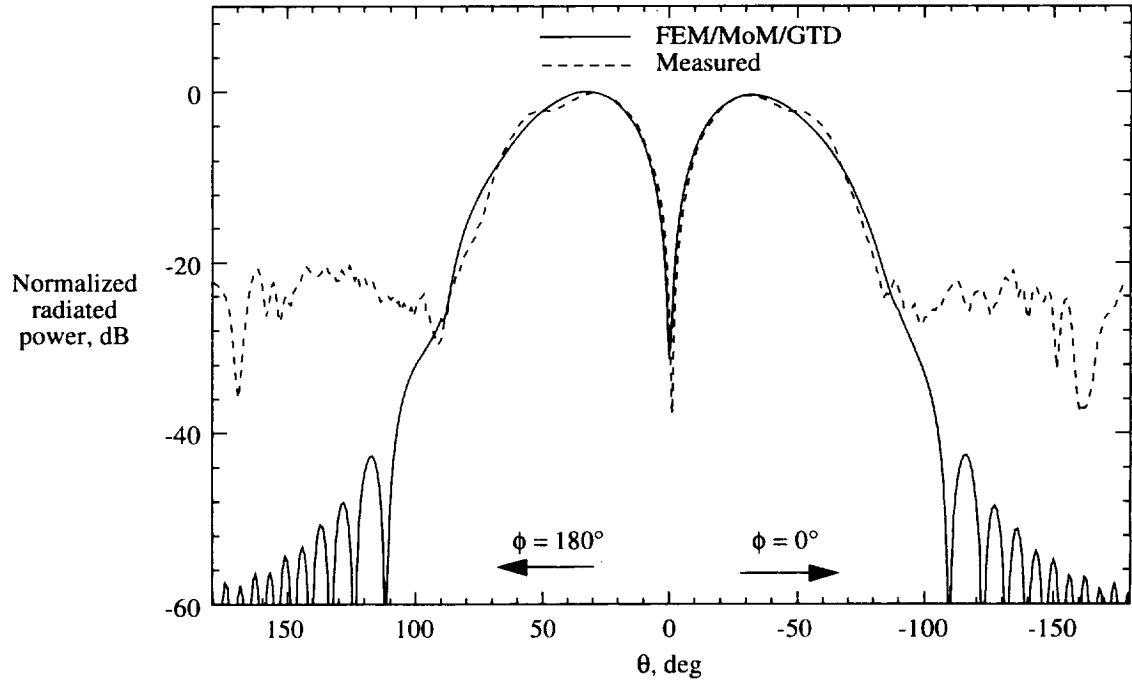


(a) Horizontal (E_θ) polarization at $\phi = 0^\circ$ and $\phi = 180^\circ$.

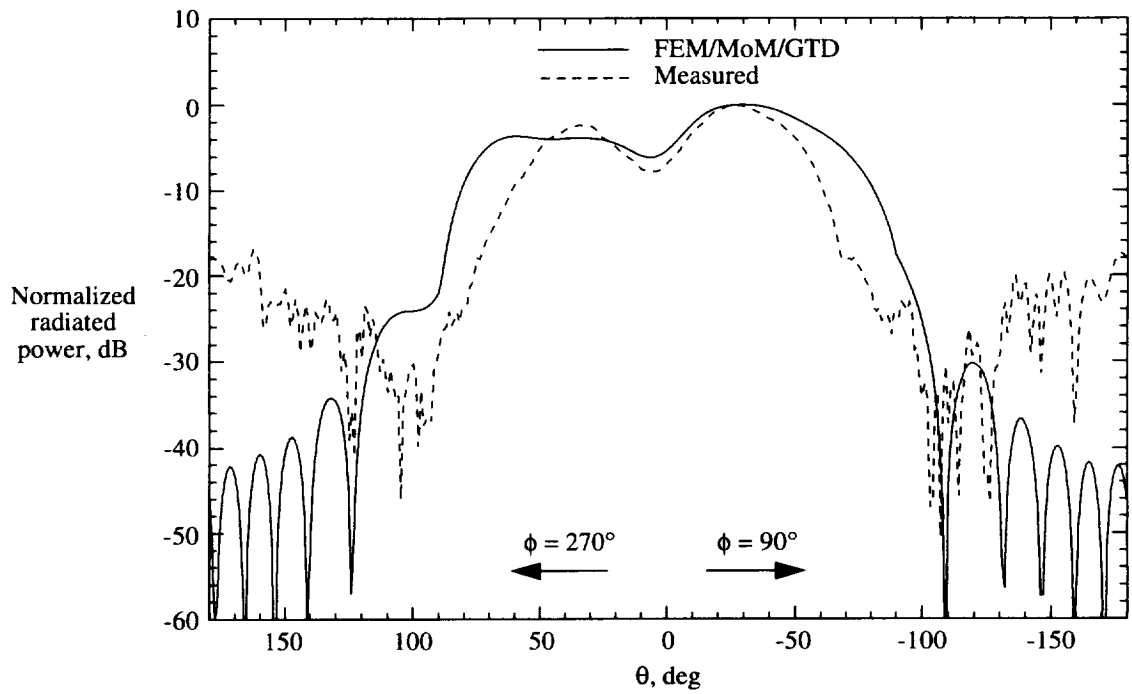


(b) Horizontal (E_θ) polarization at $\phi = 90^\circ$ and $\phi = 270^\circ$.

Figure 5. Radiation patterns of spiral antenna at 5 GHz.



(a) Vertical (E_ϕ) polarization at $\phi = 0^\circ$ and $\phi = 180^\circ$.



(b) Vertical (E_ϕ) polarization at $\phi = 90^\circ$ and $\phi = 270^\circ$.

Figure 6. Radiation patterns of spiral antenna at 5 GHz.

REPORT DOCUMENTATION PAGE			Form Approved OMB No. 0704-0188	
Public reporting burden for this collection of information is estimated to average 1 hour per response, including the time for reviewing instructions, searching existing data sources, gathering and maintaining the data needed, and completing and reviewing the collection of information. Send comments regarding this burden estimate or any other aspect of this collection of information, including suggestions for reducing this burden, to Washington Headquarters Services, Directorate for Information Operations and Reports, 1215 Jefferson Davis Highway, Suite 1204, Arlington, VA 22202-4302, and to the Office of Management and Budget, Paperwork Reduction Project (0704-0188), Washington, DC 20503.				
1. AGENCY USE ONLY (Leave blank)		2. REPORT DATE November 1996		3. REPORT TYPE AND DATES COVERED Technical Paper
4. TITLE AND SUBTITLE A Combined FEM/MoM/GTD Technique To Analyze Elliptically Polarized Cavity-Backed Antennas With Finite Ground Plane			5. FUNDING NUMBERS WU 505-64-52-04	
6. AUTHOR(S) C. J. Reddy, M. D. Deshpande, D. T. Fralick, C. R. Cockrell, and F. B. Beck				
7. PERFORMING ORGANIZATION NAME(S) AND ADDRESS(ES) NASA Langley Research Center Hampton, VA 23681-0001			8. PERFORMING ORGANIZATION REPORT NUMBER L-17552	
9. SPONSORING/MONITORING AGENCY NAME(S) AND ADDRESS(ES) National Aeronautics and Space Administration Washington, DC 20546-0001			10. SPONSORING/MONITORING AGENCY REPORT NUMBER NASA TP-3618	
11. SUPPLEMENTARY NOTES Reddy: Hampton University, Hampton, VA; Deshpande: ViGYAN, Inc., Hampton, VA; Fralick: Lockheed-Martin Engineering & Sciences Company, Hampton, VA; Cockrell and Beck: Langley Research Center, Hampton, VA.				
12a. DISTRIBUTION/AVAILABILITY STATEMENT Unclassified-Unlimited Subject Category 17 Availability: NASA CASI (301) 621-0390			12b. DISTRIBUTION CODE	
13. ABSTRACT (Maximum 200 words) Radiation pattern prediction analysis of elliptically polarized cavity-backed aperture antennas in a finite ground plane is performed using a combined Finite Element Method/Method of Moments/Geometrical Theory of Diffraction (FEM/MoM/GTD) technique. The magnetic current on the cavity-backed aperture in an infinite ground plane is calculated using the combined FEM/MoM analysis. GTD, including the slope diffraction contribution, is used to calculate the diffracted fields caused by both soft and hard polarizations at the edges of the finite ground plane. Explicit expressions for regular diffraction coefficients and slope diffraction coefficients are presented. The slope of the incident magnetic field at the diffraction points is derived and analytical expressions are presented. Numerical results for the radiation patterns of a cavity-backed circular spiral microstrip patch antenna excited by a coaxial probe in a finite rectangular ground plane are computed and compared with experimental results.				
14. SUBJECT TERMS Spiral antennas; Cavity-backed; Finite Element Method; Method of Moments; Geometrical Theory of Diffraction			15. NUMBER OF PAGES 20	
			16. PRICE CODE A03	
17. SECURITY CLASSIFICATION OF REPORT Unclassified		18. SECURITY CLASSIFICATION OF THIS PAGE Unclassified		19. SECURITY CLASSIFICATION OF ABSTRACT Unclassified
				20. LIMITATION OF ABSTRACT